Chemical Engineering & Technology

Topical issue MMPE

Manuscript ceat.201500089R1

Numerical Simulation of Wetting Phenomena with a Phase-field Method using OpenFOAM®

Xuan Cai[1], Holger Marschall[2], Martin Wörner[1,*], Olaf Deutschmann[1,3]

[1]Karlsruhe Institute of Technology, Institute of Catalysis Research and Technology, Hermann-von-Helmholtz-Platz 1, 76344 Eggenstein-Leopoldshafen, Germany

[2]Technische Universität Darmstadt, Center of Smart Interfaces, 64287 Darmstadt, Germany

[3]Karlsruhe Institute of Technology, Institute for Chemical Technology and Polymer Chemistry, Engesserstr. 20, 76131 Karlsruhe, Germany

* Corresponding author: Dr. M. Wörner, E-mail: martin.woerner@kit.edu, Phone +49 721 608 47426, Fax: +49 721 608 44805

Abstract

The phase-field method coupled with the Navier-Stokes equations is a rather new approach for scale-resolving numerical simulation of interfacial two-phase flows. Due to the diffuse nature of the interface, it is attractive for flows with moving contact lines. While the method is nowadays mainly used in finite-element in-house codes, it is our goal to implement it as finite-volume method in the open source library for computational continuum mechanics OpenFOAM® and make it freely available. In this paper, we give an overview on the governing equations and shortly discuss the numerical method. The focus of the paper is on application and validation of the code for some fundamental wetting phenomena, namely the capillary rise in a narrow channel and the spreading of a droplet on a flat surface, which is chemically either homogeneous or regularly patterned. The numerical results on static meshes are in good agreement with analytical solutions as well as experimental/numerical results from literature. We also present first three-dimensional finite-volume simulations with adaptive mesh refinement near the interface as a key element to achieve CPU-time efficient simulations.

Keywords: Capillary rise, Computational fluid dynamics, Droplet spreading, Moving contact line, Phase-field method

1 Introduction

The wetting of a liquid on solid surfaces is a crucial process in many applications in chemical industry such as coating, painting, and reactive gas-liquid flows in chemical sponge reactors. The technological improvement of these processes requires precise knowledge of wetting dynamics. Computational fluid dynamics (CFD) can be a valuable tool to gain these insights [1]. For reliable CFD simulations, it is vital to model accurately the motion of the contact line, where the moving gas-liquid interface is in contact with the solid surface. In this context, conventional sharp-interface hydrodynamic models suffer from a paradox between the moving contact line and no-slip boundary condition at the solid wall [2], which leads to a non-integrable viscous stress singularity at the moving contact line. Various methods have been proposed such as the precursor film model [3] and the slip model [4] to resolve this problem. A recent detailed overview on numerical simulations of flows with moving contact lines is provided in the review by Sui et al. [5].

Among the various methods for interfacial simulations of two-phase flows [6], the phase-field method is one of the most promising approaches for handling moving contact lines. It relies on a diffuse interface model [7] that treats the interface between two immiscible fluids as a transition region of small but finite width, endowed with surface tension [8]. Based on fluid free energy, the method can be traced back to van der Waals a century ago [9]. In recent years, the phase-field method has become popular not only for numerical simulation of moving contact lines [10] and related wetting phenomena [11] but also for capillary two-phase flows in general [7]. In our study, the most significant feature of this method is that it allows motion of the contact line in combination with a no-slip boundary condition at a solid wall via a diffusive mechanism induced by a chemical potential gradient [12].

In this paper, we shortly present the phase-field method developed and implemented by the authors using the free open source library for computational continuum mechanics OpenFOAM®. The method is novel in two respects. Namely, it is the first finite volume method based implementation of phase-field method for two-phase wetting processes with three-dimensional adaptive mesh refinement near the interface. Second, it is the first application of the phase-field method for wetting processes

using real air-water density and viscosity ratios. The aim of this paper is, first, to validate the method for some fundamental wetting phenomena and, second, to demonstrate its capabilities concerning physically more complex wetting dynamics. In Section 2, we introduce the mathematical formulation and the numerical method. Section 3 presents simulations on capillary rise and droplet spreading on a flat surface, and highlights the method's capability regarding adaptive mesh refinement and wetting on chemically heterogeneous substrates.

2 Mathematical formulation

In OpenFOAM®, the governing equations are solved in dimensional form. In this paper, we present all simulation results in non-dimensional terms, based on suitable dimensionless physical or geometrical groups. For consistency, we present the governing equations in non-dimensional form as well. Similar to [13, 14], we base our normalization on a reference length scale, L_{ref}, and a reference velocity scale, U_{ref}, which are chosen problem-dependent.

2.1 Phase-field approach for interface evolution

In the phase-field method, the phase distribution of two phases A and B is described by an order parameter, C. Here we take C as the difference in volumetric phase fractions of both phases, i.e. $C = \alpha_{\mathrm{A}} - \alpha_{\mathrm{B}}$. Thus, C takes distinct values $C_{\mathrm{A}} = 1$ and $C_{\mathrm{B}} = -1$ in the bulk phases and varies rapidly but smoothly in a thin transition layer (the diffuse interface). In equilibrium, the variation $-0.9 \le C \le 0.9$ occurs over a distance of 4.164ε [8], where ε is an interfacial thickness parameter which we denote here as interfacial width.

The interface dynamics is governed by an evolution equation for C, the convective Cahn-Hilliard equation, which reads in non-dimensional form

$$\frac{\partial C}{\partial \tau} + (\mathbf{u} \cdot \nabla) C = \frac{1}{Pe_C} \nabla^2 \phi \tag{1}$$

Here, $\tau = t \cdot U_{\mathrm{ref}} / L_{\mathrm{ref}}$ denotes the non-dimensional time, ∇ is the non-dimensional Nabla operator, $\mathbf{u}$ the non-dimensional velocity field, and

$$\phi = C^3 - C - Cn^2 \nabla^2 C \tag{2}$$

is the non-dimensional chemical potential [14]. The term on the right-hand-side of Eq. (1) provides a diffusive mechanism for motion of the contact line at a no-slip wall. Based on the wall free energy formulation at local equilibrium, one can derive the following boundary condition to account for the wettability of the solid substrate [15]

$$\hat{\mathbf{n}}_{\mathrm{s}} \cdot \nabla C = \frac{\sqrt{2}}{2} \frac{\cos\theta_{\mathrm{e}}}{Cn} (1 - C^2) \tag{3}$$

Here, θ_{e} is the equilibrium (static) contact angle and $\hat{\mathbf{n}}_{\mathrm{s}}$ is the unit vector normal to the solid surface.

In the above equations, two phase-field method specific non-dimensional parameters appear. $Pe_C = \sqrt{8/9} L_{\mathrm{ref}} U_{\mathrm{ref}} \varepsilon / \kappa\gamma$ is a "Peclet number" for the order parameter, where κ is the mobility and γ the interfacial energy. Pe_C is a measure for the ratio between the advective and diffusive transport of C and quantifies the diffusion process that governs the motion of the contact line. The Cahn number $Cn = \varepsilon / L_{ref}$ relates the interfacial width to the macroscopic length scale. We consider Pe_C and Cn as numerical parameters of our phase-field method for interface capturing, which can be varied via κ and ε. The choice of Cn is influenced, at least, by numerical accuracy, efficiency, and stability [15]. The value of Pe_C affects the temporal evolution of the simulation but has – when chosen in an appropriate range [8] – no influence on the steady results.

2.2 Equations governing the fluid flow

In this paper, we consider two immiscible, incompressible, isothermal Newtonian fluids. Hence, we can describe the two-phase flow by the following non-dimensional single-field formulation of the Navier-Stokes equations

$$\nabla \cdot \mathbf{u} = 0 \tag{4}$$

$$\rho_C Re \left(\frac{\partial \mathbf{u}}{\partial \tau} + (\mathbf{u} \cdot \nabla)\mathbf{u} \right) = -\nabla P + \nabla \cdot \left[\mu_C \left(\nabla\mathbf{u} + (\nabla\mathbf{u})^{\mathrm{T}} \right) \right] + \mathbf{f}_{\mathrm{st}} + \mathbf{f}_{\mathrm{b}} \tag{5}$$

The density and viscosity fields depend on the order parameter as

$$\rho_C = \frac{1}{2}\left((C+1) - \frac{\rho_{\mathrm{B}}}{\rho_{\mathrm{A}}}(C-1) \right), \quad \mu_C = \frac{1}{2}\left((C+1) - \frac{\mu_{\mathrm{B}}}{\mu_{\mathrm{A}}}(C-1) \right) \tag{6}$$

where $\rho_{A/B}$ and $\mu_{A/B}$ are the density and viscosity of the pure phases. In Eq. (5), $P = p / \mu_A U_{ref} L_{ref}^{-1}$ denotes the non-dimensional pressure field. The surface tension force and buoyancy force in Eq. (5) are

$$\mathbf{f}_{st} = -\frac{1}{Ca \cdot Cn} C \nabla \phi(C) \,,\ \mathbf{f}_b = -\frac{1}{2}\frac{Eo}{Ca}(C+1)\hat{\mathbf{e}}_z \tag{7}$$

There are three dimensionless physical groups in the above equations: the Reynolds number $Re = \rho_A L_{ref} U_{ref} / \mu_A$, the capillary number $Ca = \sqrt{8/9}\mu_A U_{ref} / \gamma$, and the Eötvös number $Eo = (\rho_A - \rho_B) g L_{ref}^2 / \gamma$, where g is the gravitational acceleration. Eqs. (6) and (7) couple the Navier-Stokes Eq. (5) with the Cahn-Hilliard Eq. (1). The latter depends in return on the velocity field $\mathbf{u}$, which is obtained from solution of the Navier-Stokes equation. Finally, we remark that the Cahn number enters in the definition of the surface tension force while the Peclet number Pe_C is absent in the Navier-Stokes equations.

2.3 Numerical aspects

We implemented the above system of equations in OpenFOAM® in order to solve it numerically with a finite-volume method. Spatial derivatives are approximated by a high-resolution scheme (Gauss Gamma) and time integration is performed by a second-order two time-level backward scheme (Gear's method). The time step is chosen such that the maximum Courant number is 0.1. For further details we refer to [16] and [17]. In [16], we also verified and validated the code for several test problems and studied the influence of Pe_C, Cn and the grid resolution. The latter showed a good compromise between accuracy and computational cost if the interface is resolved by 4-8 mesh cells and $Cn = 0.01$. In [17] we detail on a robust treatment of large density and viscosity ratios as well as the enforcement of boundedness and conservation properties, e.g. by means of a second-order implicit block-coupled solution strategy, in which the 4th order Cahn-Hilliard phase-field equation is split into two Helmholtz-type equations and then solved simultaneously within one linear solver sweep. Similar to [18], we implemented a relative density flux in the momentum equation due to diffusion of the two-phase components to achieve volume conservation for two-phase flows with large density ratios.

3 Results and discussion

In this section, we apply the code to two phenomena with moving contact lines: capillary rise and spreading of a partially wetting droplet on a flat surface. For validation, we start with static-mesh simulations for planar and axisymmetric problems, where analytical solutions or experimental data are available for comparison. In order to demonstrate the potential of the method for problems of increasing computational and physical complexity, we perform three-dimensional (3D) simulations with adaptive mesh refinement and consider the spreading on a chemically patterned surface. Concerning the initial conditions, we start all simulations with both phases at rest and a smooth hyperbolic tangent equilibrium distribution of C in the interfacial region according to the respective value of Cn. For analyzing the results, we take $C = 0$ as position of the interface.

3.1 Equilibrium height of capillary rise

In this test case, we reproduce the capillary rise of a fluid A in the gap between two vertical parallel plates where it displaces fluid B. The ratio between the final height, h, of the column and the distance of the plates, d, is

$$\frac{h}{d} = \frac{2\sigma\cos(\theta_e)}{\rho_A g d^2} \tag{8}$$

The fluids in our simulations are water ($\rho_A = 998\,\mathrm{kg\,m^{-3}}$, $\mu_A = 10^{-3}\,\mathrm{Pa\,s}$) and air ($\rho_B = 1.2\,\mathrm{kg\,m^{-3}}$, $\mu_B = 1.81\times10^{-5}\,\mathrm{Pa\,s}$, $\gamma = 0.072\,\mathrm{J\,m^{-2}}$). The channel width is $d = L_{ref} = 2\,\mathrm{mm}$ and $g = 9.81\,\mathrm{m\,s^{-2}}$. The values of the Cahn and Peclet numbers are $Cn = 0.025$ and $Pe = 327$, respectively. We use a uniform isotropic static mesh and resolve the plate distance d by 40 mesh cells. This corresponds to approximately four mesh cells for the region $-0.9 \le C \le 0.9$. In this paper, all flows evolve to static state. Thus, there is no characteristic velocity and we define U_{ref} indirectly by setting $Re = 1$.

Fig. 1 a-d illustrates the time dependent simulation results for $\theta_e = 45°$. Initially, the channel is filled with air while the water is in the container and the interface is flat (Fig. 1 a). When the simulation starts, the wall adhesion force causes the water to creep up along the wall, to meet the prescribed

equilibrium contact angle (Fig. 1 b). Then a pressure jump arises across the curved interface, which drives the water further upward (Fig. 1 c). This continues until the capillary force is in balance with the gravity force (Fig. 1 d). In this study, we performed simulations for five different values of θ_e in the range $30° \le \theta_e \le 60°$. For all cases, the computed steady column height (evaluated midway between the channel centerline and the right plate) is in good agreement with the analytical solution in Eq. (8) as shown in Fig. 1 e.

(Figure 1)

3.2 Equilibrium shape of a planar droplet

We now consider the spreading of a droplet on a flat homogeneous surface and compare characteristic dimensions of the computed equilibrium droplet shape with analytical solutions. We start from a planar semi-circular droplet with initial radius $R_0 = D_0 / 2$ and initial contact angle $\theta_0 = 90°$ (Fig. 2 a). We quantify the numerical results for a given value of θ_e by the equilibrium droplet height H and base length L (Fig. 2 b). In our 2D simulations, the size of the computational domain is $3D_0 \times D_0$ and we resolve D_0 by 50 mesh cells. Furthermore, we use $L_{ref} = D_0$, $Cn = 0.01$ and $Pe_C = 1000$.

We first consider the case when gravity forces are negligible ($Eo = 0$) so that capillarity is the only driving force. In this case, the droplet is spreading for $\theta_e < \theta_0$ and is dewetting for $\theta_e > \theta_0$. In both cases, the equilibrium shape is a circular cap. By geometrical constraints it follows

$$L_0 = 2R_0 \sin\theta_e \sqrt{\frac{\pi}{2(\theta_e - \sin\theta_e \cos\theta_e)}} \tag{9}$$

$$H_0 = R_0(1-\cos\theta_e)\sqrt{\frac{\pi}{2(\theta_e - \sin\theta_e \cos\theta_e)}} \tag{10}$$

Here, we performed numerical simulations for seven distinct values of θ_e in the range $45° \le \theta_e \le 135°$. In Fig. 2 c we compare the computed values for H / R_0 and L / R_0 with the analytical solutions from Eq. (9) and (10). The agreement is very good, both for hydrophilic and hydrophobic situations.

(Figure 2)

In the case $Eo > 0$, the droplet spreads on the solid surface due to the combined effect of capillary and gravitational forces. In the final stage, gravity tends to spread out the droplet further while the capillary force tends to maintain a circular cap. For $Eo \gg 1$, the gravity force dominates and the droplet forms a puddle. Also in the limit $Eo \to \infty$ the equilibrium height of the droplet is known analytically [19] and given by

$$H_\infty = \frac{2R_0}{\sqrt{Eo}} \sin\left(\frac{\theta_e}{2}\right) \tag{11}$$

Similar to numerical studies for other methods [20, 21], we performed simulations for one specific value of the equilibrium contact angle ($\theta_e = 60°$) and seven distinct values of the Eötvös number in the range $0.01 \le Eo \le 10$. In Fig. 3 we plot the final droplet height, H, normalized by H_0 from Eq. (10) as a function of Eo. For $Eo \le 0.1$ the simulation results agree with the asymptotic solutions given by Eq. (10), while for $Eo \ge 5$ they agree with the asymptotic solution given by Eq. (11). At $Eo \approx 1$ there is a transition between both regimes. The inset graphics in Fig. 3 show the equilibrium droplet shape for $Eo = 0.1$ (a circular cap), $Eo = 1$ (an elongated circular cap) and $Eo = 10$ (a puddle).

(Figure 3)

3.3 Spreading dynamics on a homogeneous surface

We now turn to the spreading dynamics of a partially wetting droplet on a flat surface. In a preliminary study, we neglect gravity ($Eo = 0$) so that spreading is driven by capillary forces only. We further assume that the velocities are so small that inertial forces are negligible, too, and set the density ratio between the ambient fluid and the droplet to unity. As reference length we choose $L_{ref} = D_0$, where D_0 is the initial drop diameter. For presentation of the transient simulation results, we scale time by the capillary time scale $t_{cap} = \mu_A D_0 / \gamma$.

3.3.1 Axisymmetric simulations

To investigate the dynamic wetting process, we turn from planar to axisymmetric geometry and compare the results with experimental data of Zosel [22]. He studied the spreading of droplets of fluids with different viscosity on a flat surface and recorded the instantaneous droplet base radius. The droplet diameters were in the range $2.4-3\,\mathrm{mm}$ so that gravitational effects are small. The drops were released with almost spherical shape and low kinetic energy.

For comparison, we selected one specific experiment with an equilibrium contact angle $\theta_e = 58°$ where a very viscous drop of polyisobutylene ($D_0 = 2.6\,\mathrm{mm}$, $\mu_A = 25\,\mathrm{Pa\,s}$, $\rho_A = 920\,\mathrm{kg\,m^{-3}}$, $\gamma = 0.0426\,\mathrm{J\,m^{-2}}$) spreads on a polymer surface (PTFE). The viscosity ratio between the ambient air and the droplet is $\lambda_\mu = \mu_B / \mu_A \approx 10^{-6}$. In our simulations, we set $\lambda_\mu = 0.05$ in order to save computational effort. A sensitivity study on λ_μ showed that a further decrease does not affect the results significantly. In our axisymmetric simulations, the size of the computational domain is $2D_0 \times 1.5D_0$. We resolve D_0 by 100 mesh cells and start from $\theta_0 = 170°$. The Cahn number is $Cn = 0.01$ and we compare simulations for two values of the Peclet number, $Pe_C = 200$ and 1000.

In Fig. 4 we compare the time evolution of the computed base radius of the drop with the experimental data [22]. Good agreement is achieved, especially at the later spreading stage. As Pe_C decreases, the base radius changes faster, and the result gets slightly closer to the experimental data. This is reasonable since in the phase-field method the contact line moves by diffusion. Thus, a stronger diffusion (i.e. a smaller value of Pe_C) leads to a faster spreading.

We also investigated the influence of a dynamic contact angle on the spreading dynamics. Following [12, 23], we included in Eq. (3) for this purpose a time-dependent term $\partial C / \partial t$ multiplied by an phenomenological parameter. However, the effect of the dynamic contact model on the spreading dynamics turned out to be negligible, a results that can be attributed to the high drop viscosity [23].

(Figure 4)

3.3.2 3D simulations with adaptive mesh refinement

A key element to achieve high numerical accuracy with moderate computational cost in 3D is the use of local adaptive mesh refinement (AMR). This procedure allows providing significantly higher mesh densities where most needed – at the interface. This is particularly important for diffuse interface simulations. There, the interface must be thin enough to converge to the sharp-interface limit while its thickness must be adequately resolved so that interfacial effects are computed accurately [24].

In this section, we demonstrate the capabilities of the method with respect to 3D AMR. The AMR is handled by the class *dynamicRefineFvMesh* in the OpenFOAM® C++ library. From the initial state, we set a two-level mesh refinement for the interface region compared with the bulk region (Fig. 5). For each time step during the simulation, the mesh is refined adaptively in regions where $-0.9 < C < 0.9$.

In Fig. 6 we illustrate the spreading process for $\theta_e = 75°$. Starting from the initial contact angle $\theta_0 = 170°$, the droplet is spreading out as time proceeds and approaching to the final state with the prescribed equilibrium contact angle. A similar simulation was performed for $\theta_e = 90°$.

(Figures 5 and 6)

To verify the 3D AMR simulations, we compare the results with those from static-mesh axisymmetric simulations (cf. Sect. 3.3.1) for identical physical and numerical parameters ($Ca = 0.94$, $\lambda_\mu = 0.1$, $Cn = 0.01$, $Pe_C = 1000$). In addition, the mesh resolution in the diffuse interface region is the same. Away from the interface, the cell width in the 3D AMR simulations is (in each direction) by a factor of four larger than in the static mesh axisymmetric simulations. In Fig. 7 we compare the time evolution of the normalized drop base radius and find a close agreement, both for $\theta_e = 75°$ and $90°$. This figure also demonstrates the effect of the substrate wettability on the spreading process: from the very beginning the droplet spreads faster on the substrate with higher wettability (smaller θ_e). The reason is that the spreading is driven by the mismatch between θ_0 and θ_e so that a larger difference between both angles leads to a faster spreading.

(Figure 7)

3.4 Droplet spreading on a chemically patterned surface

So far, we considered the spreading on a chemically homogeneous substrate where θ_e is uniform. We now extend the study to a chemically heterogeneous substrate, patterned with alternating hydrophilic and hydrophobic stripes. The purpose for considering this test case is to demonstrate that the method is able to reproduce characteristic phenomena such as anisotropic spreading and stick-slip motion.

To allow for a qualitative comparison with literature, we consider a similar scenario as Jansen et al. [25] who used the lattice Boltzmann method (LB). The base surface is made up of hydrophilic SiO_2 stripes ($\theta_e = 40°$) and hydrophobic perfluordecyltrichlorosilane (PFDTS) stripes ($\theta_e = 110°$). The stripe width ratio is $w_{\mathrm{PFDTS}} / w_{\mathrm{SiO_2}} = 0.5$ and we use four mesh cells for each SiO_2 stripe and two for each PFDTS stripe. We set $Ca = 0.94$, $Pe_C = 1000$, $Cn = 0.02$, $\lambda_\mu = 0.1$.

Initially, the 3 microliter polyisobutylene droplet just touches the surface (Fig. 8 a). Subsequently, it wets the substrate (Fig. 8 b) but in a manner different from that for a homogeneous surface: due to the stripe pattern, the droplet spreads preferentially along the stripes while its motion in direction perpendicular to them is hindered (Fig. 8 c). Finally, the droplet adopts an elongated equilibrium shape with the larger axis in direction of the stripes (Fig. 8 d).

(Figure 8)

In Fig. 9 we display the time evolution of the footprints of the droplet in both directions. The final traveling distance of the moving contact line is larger along the stripes than perpendicular to them. Furthermore, the contact line advances smoothly along the stripes, while in the perpendicular direction it moves in a stick-slip manner. This behavior can be explained as follows. Perpendicular to the stripes, the contact line has to overcome a series of high-energy barriers when it passes through hydrophobic stripes. This results in the stick-slip-like motion (i.e., the pinning behavior) and limited spreading in this direction. In contrast, such discrete energy barriers do not exist along the stripes. In this direction, the contact line travels therefore continuously and the droplet spreads over a greater distance.

(Figure 9)

We now compare our results with Jansen et al. [25] who performed experiments and LB simulations. In the experiment, the final static droplet encompassed around 77 stripes, each of which is extremely narrow in width. Resolving so many stripes in a 3D simulation is computationally prohibitive for current numerical methods. Therefore, the LB simulations in [25] were made for wider stripes and the drop spans only a few of them. In our simulations, we made the same approach. Unfortunately, in [25] no physical properties are given for the LB simulations but only dimensionless values of the drop and gas density. Furthermore, the LB method in [25] can only be applied for fluids that have roughly the same kinematic viscosity. Since the information on the LB simulations is not sufficient to recalculate the case with our method, we considered instead the polyisobutylene droplet from Zosel's experiment (cf. Section 3.3). Due to the different physical systems, one may compare the LB and phase-field simulation results only qualitatively.

Fig. 10 shows the evolution of the droplet shape from a bottom-view. At the initial stage, the droplet is just slightly elongated (Fig. 10a, e and i) and the effect of the patterned surface is not significant. As time proceeds, the drop preferentially spreads in direction of the stripes and its shape

further elongates toward its final state (Fig. 10d, h and l). The results of our phase-field simulations are in good qualitative agreement with the LB results.

The contact line profile at the longer ends of the droplet is different in the experiment (where it is smooth) and in the simulations (where it is corrugated and wave like). This relates to the different number of stripes covered by the droplet. Such corrugation patterns of the contact line were also observed in other numerical studies where the droplet spans a small number of stripes [26].

(Figure 10)

4 Summary and outlook

In this paper, we have presented a phase-field method for interface resolving numerical simulations of two-phase flows with OpenFOAM® and applied it to representative capillary flows with moving contact lines. For both, the capillary rise between parallel plates and droplet wetting on a flat surface the computed equilibrium shape of the interface agrees well with analytical solutions. Concerning droplet-spreading dynamics, our time dependent simulation results are in good agreement with literature data, both for a chemically homogeneous and a chemically patterned surface. We also demonstrated the use of adaptive mesh refinement at the interface. This altogether shows that the presented phase-field method is a reliable and promising numerical method for general capillary two-phase flows involving moving contact lines.

We now advance the method in OpenFOAM® towards a volume-conservative and bounded phase-field framework incorporating both Cahn-Hilliard and Allen-Cahn equations [17]. Next, we will validate the code with respect to a wall energy relaxation model for dynamic contact angles in rapid wetting processes and extend our method to contact angle hysteresis.

Acknowledgement

We gratefully acknowledge the funding by Helmholtz Energy Alliance “Energy-efficient chemical multiphase processes” (HA-E-0004). The first and the third author would like to thank Prof. Hocine Alla and Dipl.-Math. Marouen Ben Said for stimulating discussions.

Symbols used

Ca	[-]	Capillary number
Cn	[-]	Cahn number
d	[m]	distance between parallel vertical plates
D_0	[m]	initial drop diameter
$\hat{\mathbf{e}}_z$	[-]	unit normal vector in vertical direction
Eo	[-]	Eötvös number
H	[m]	droplet height
H_0	[m]	equilibrium droplet height for $Eo = 0$
H_∞	[m]	equilibrium droplet height for $Eo \to \infty$
L	[m]	droplet base length
L_{ref}	[m]	reference length scale
$\hat{\mathbf{n}}_s$	[-]	unit normal vector to the solid surface
P	[-]	non-dimensional pressure
Pe_C	[-]	Peclet number in Cahn-Hilliard equation
R_0	[m]	initial drop radius
Re	[-]	Reynolds number
t	[s]	time
t_{cap}	[s]	capillary time scale, $t_{\mathrm{cap}} = \mu_{\mathrm{A}} D_0 / \gamma$
U_{ref}	[m s^{-1}]	reference velocity scale
$\mathbf{u}$	[-]	velocity field normalized by U_{ref}

Greek symbols		
α	[-]	volume fraction
γ	[J m^{-2}]	interfacial energy
ε	[m]	interfacial width
κ	[m^3 s kg^{-1}]	mobility
λ_μ	[-]	viscosity ratio
μ	[Pa s]	dynamic viscosity
ϕ	[-]	non-dimensional chemical potential
ρ	[kg m^{-3}]	density
θ	[°]	contact angle
τ	[-]	non-dimensional time

Subscripts	
A	phase A
B	phase B
e	equilibrium
ref	reference value

References

[1] H. Alla, S. Freifer, T. Roques-Carmes, *Colloids and Surfaces A: Physicochemical and Engineering Aspects* **2011,** *386 (1-3)*, 107-115.
[2] C. Huh, L. E. Scriven, *J Colloid Interf Sci* **1971,** *35 (1)*, 85-101.
[3] P. G. de Gennes, *Rev Mod Phys* **1985,** *57 (3)*, 827-863.
[4] M. Renardy, Y. Renardy, J. Li, *J Comput Phys* **2001,** *171 (1)*, 243-263.
[5] Y. Sui, H. Ding, P. D. M. Spelt, *Annu Rev Fluid Mech* **2014,** *46 (1)*, 97-119.
[6] M. Wörner, *Microfluid Nanofluid* **2012,** *12 (6)*, 841-886.
[7] D. M. Anderson, G. B. McFadden, A. A. Wheeler, *Annu Rev Fluid Mech* **1998,** *30*, 139-165.
[8] D. Jacqmin, *J Comput Phys* **1999,** *155 (1)*, 96-127.
[9] J. D. v. d. Waals, *Verhandel/Konink Akad Weten* **1879,** *1*, 8.
[10] P. T. Yue, C. F. Zhou, J. J. Feng, *J Fluid Mech* **2010,** *645*, 279-294.
[11] M. Ben Said et al., *Langmuir* **2014,** *30 (14)*, 4033-4039.
[12] D. Jacqmin, *J Fluid Mech* **2000,** *402*, 57-88.
[13] V. V. Khatavkar, P. D. Anderson, H. E. H. Meijer, *J Fluid Mech* **2007,** *572*, 367-387.
[14] A. Carlson, M. Do-Quang, G. Amberg, *Int J Multiph Flow* **2010,** *36 (5)*, 397-405.
[15] W. Villanueva, G. Amberg, *Int J Multiph Flow* **2006,** *32 (9)*, 1072-1086.
[16] X. Cai, M. Wörner, O. Deutschmann, in *7th Open Source CFD Int Conf (available online at http://www.opensourcecfd.com/conference2013/proceedings-day-2)* Hamburg, Germany **2013**.
[17] H. Marschall, X. Cai, M. Wörner, O. Deutschmann, **2015**, Conservative finite volume discretization of the two-phase Navier-Stokes Cahn-Hilliard and Allen-Cahn equations on general grids with applications to dynamic wetting, in preparation.
[18] H. Ding, P. D. M. Spelt, C. Shu, *J Comput Phys* **2007,** *226 (2)*, 2078-2095.
[19] P. G. de Gennes, F. Brochard-Wyart, D. Quéré, *Capillarity and wetting phenomena: drops, bubbles, pearls, waves*. Springer, New York, **2004**.
[20] Y. M. Chen, R. Mertz, R. Kulenovic, *Int J Multiph Flow* **2009,** *35 (1)*, 66-77.
[21] J. B. Dupont, D. Legendre, A. M. Morgante, *J Fuel Cell Sci Tech* **2011,** *8 (4)*, 041008-1 - 041008-7.
[22] A. Zosel, *Colloid Polym Sci* **1993,** *271 (7)*, 680-687.
[23] A. Carlson, M. Do-Quang, G. Amberg, *Phys Fluids* **2009,** *21 (12)*, 121701-1- 121701-4.
[24] C. Zhou et al., *J Comput Phys* **2010,** *229 (2)*, 498-511.
[25] H. P. Jansen et al., *Phys Rev E* **2013,** *88 (1)*, 013008.
[26] F. J. M. Ruiz-Cabello et al., *Langmuir* **2009,** *25 (14)*, 8357-8361.

Figure legends

Fig. 1: Capillary rise of water into a planar vertical channel ($d = 2\,\mathrm{mm}$, $\theta_e = 45°$) for four instants in time: (a) initial state, (b) 3 ms, (c) 30 ms, (d) 100 ms (final state). (e) Comparison of simulated and analytical final height for different values of θ_e.

Fig. 2: (a) Initial shape of the droplet released on the surface. (b) Equilibrium shape of the droplet. (c) Comparison of simulated and analytical spreading length L and height H for different values of the equilibrium contact angle θ_e.

Fig. 3: Normalized droplet height as function of the Eötvös number for $\theta_e = 60°$. The insets show the final droplet shape for the respective Eötvös number.

Fig. 4: Comparison of the temporal evolution of the computed droplet's base radius with experimental data [22] ($\theta_e = 58°$).

Fig. 5: (a) 3D AMR simulation of droplet spreading (one-quarter geometry, hexahedral mesh) on a flat substrate at the initial state. (b) Close-up view of the region with two-level AMR around the interface.

Fig. 6: 3D simulation of droplet spreading on a flat substrate ($\theta_e = 75°$) with AMR near the interface. Visualization of the droplet shape for different instants in time: (a) $t = 0$, $\theta_0 = 170°$ (initial state), (b) $t / t_{cap} = 2$, (c) $t / t_{cap} = 8$, (d) $t / t_{cap} = 30$ (equilibrium shape).

Fig. 7: Comparison of temporal evolution of droplet's base radius in 2D static mesh axisymmetric simulations and 3D AMR simulations.

Fig. 8: Simulation of droplet spreading on a chemically patterned substrate (dark stripes: $\theta_e = 40°$, light stripes: $\theta_e = 110°$). The spreading process starts from initial state $t = 0$ (a), via $t / t_{cap} = 40$ (b) and $t / t_{cap} = 200$ (c), till $t / t_{cap} = 1000$ (d) where the droplet reaches the equilibrium state.

Fig. 9: Temporal evolution of the base radius of the droplet in direction parallel and perpendicular to the stripes.

Fig. 10: Time evolution of the droplet shape from bottom-view. (a)-(h): Experiment and LB simulation. Reprinted figure with permission from H.P. Jensen et al., Phys Rev E 88, 013008 (2013) Copyright (2013) by the American Physical Society. (i)-(l): Present results. The numbers at the bottom left corner in subfigures (e)-(h) indicate the time step in the LB simulation while those in subfigures (i) – (l) denote t / t_{cap}.

G**raphical abstract**

A phase-field method for interface resolving numerical simulations of two-phase flows is presented and implemented in OpenFOAM®. The method is validated for several capillary flows with moving contact lines and is used to study dynamic droplet spreading on a flat surface by three-dimensional simulations with adaptive mesh refinement near the interface.

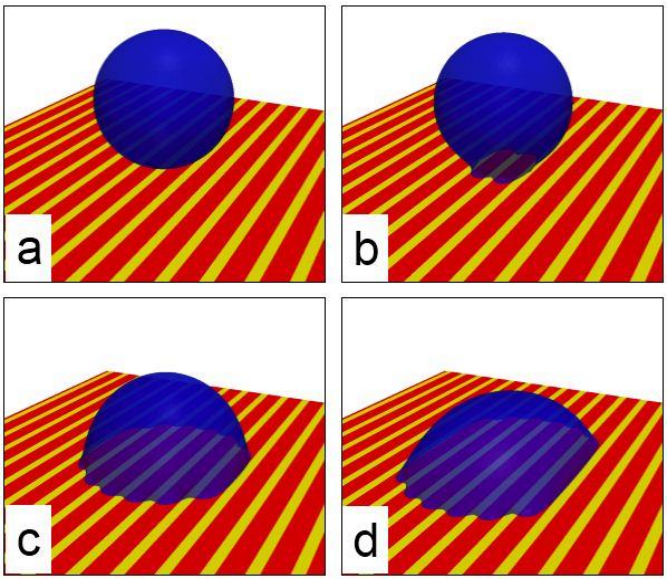

Figures

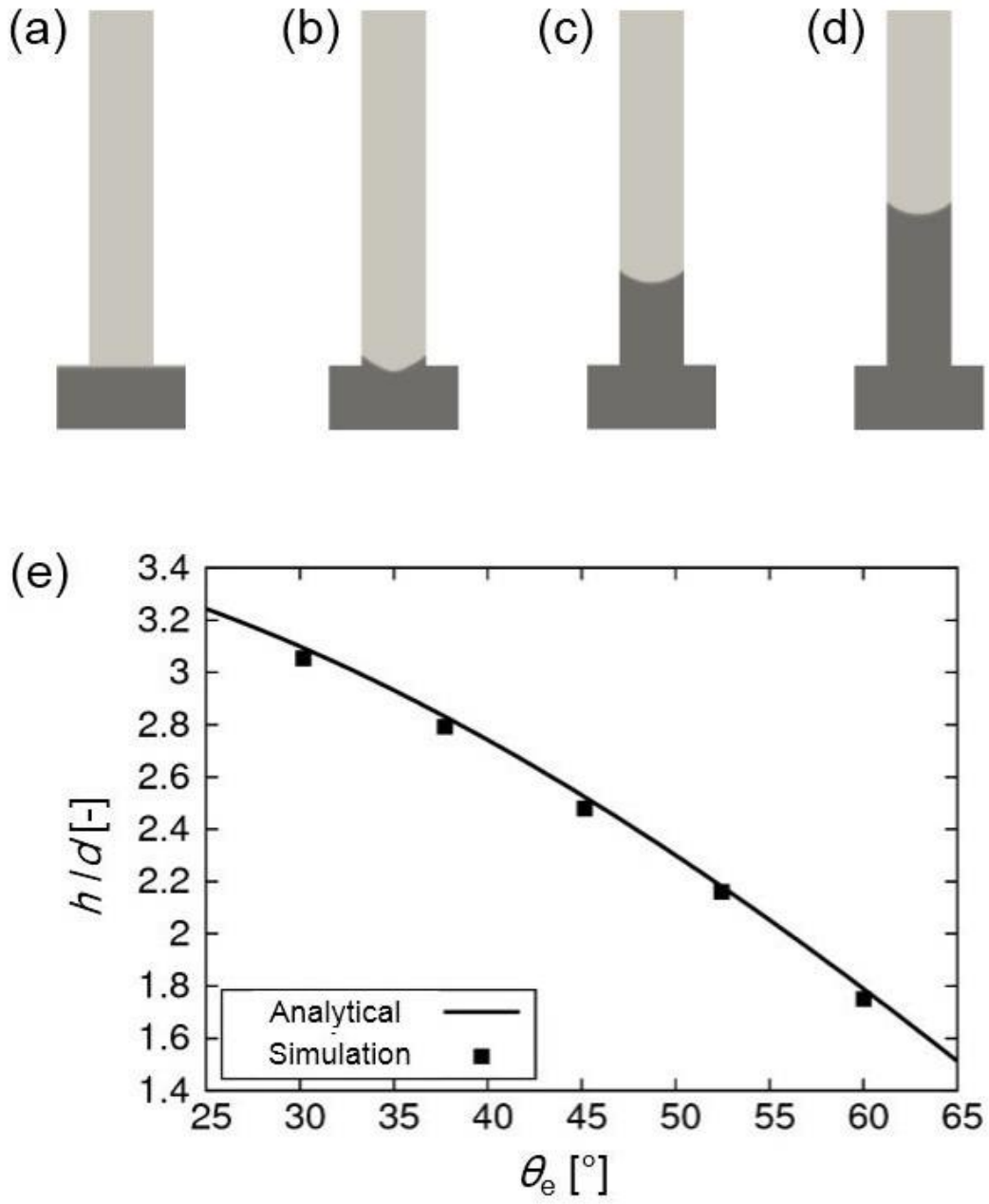

Fig. 1: Capillary rise of water into a planar vertical channel ($d = 2\,\mathrm{mm}$, $\theta_e = 45°$) for four instants in time: (a) initial state, (b) 3 ms, (c) 30 ms, (d) 100 ms (final state). (e) Comparison of simulated and analytical final height for different values of θ_e.

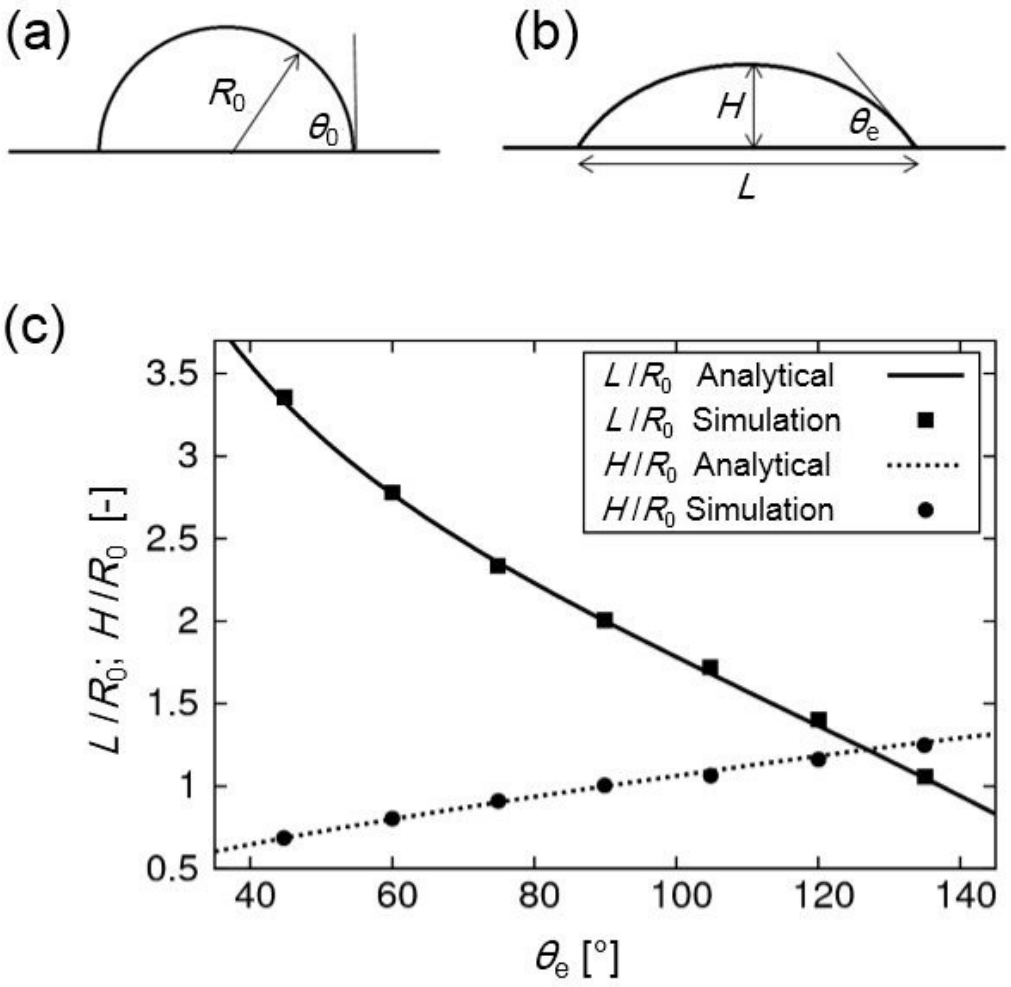

Fig. 2: (a) Initial shape of the droplet released on the surface. (b) Equilibrium shape of the droplet. (c) Comparison of simulated and analytical spreading length L and height H for different values of the equilibrium contact angle θ_e.

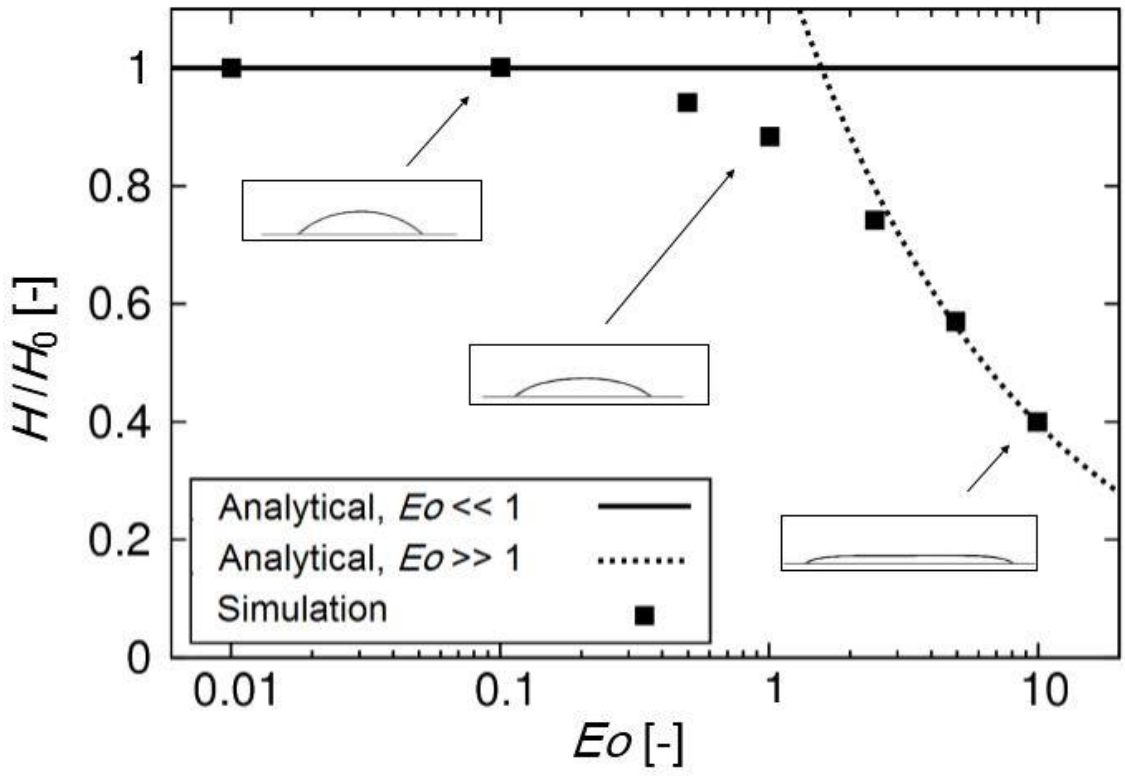

Fig. 3: Normalized droplet height as function of the Eötvös number for $\theta_e = 60°$. The insets show the final droplet shape for the respective Eötvös number.

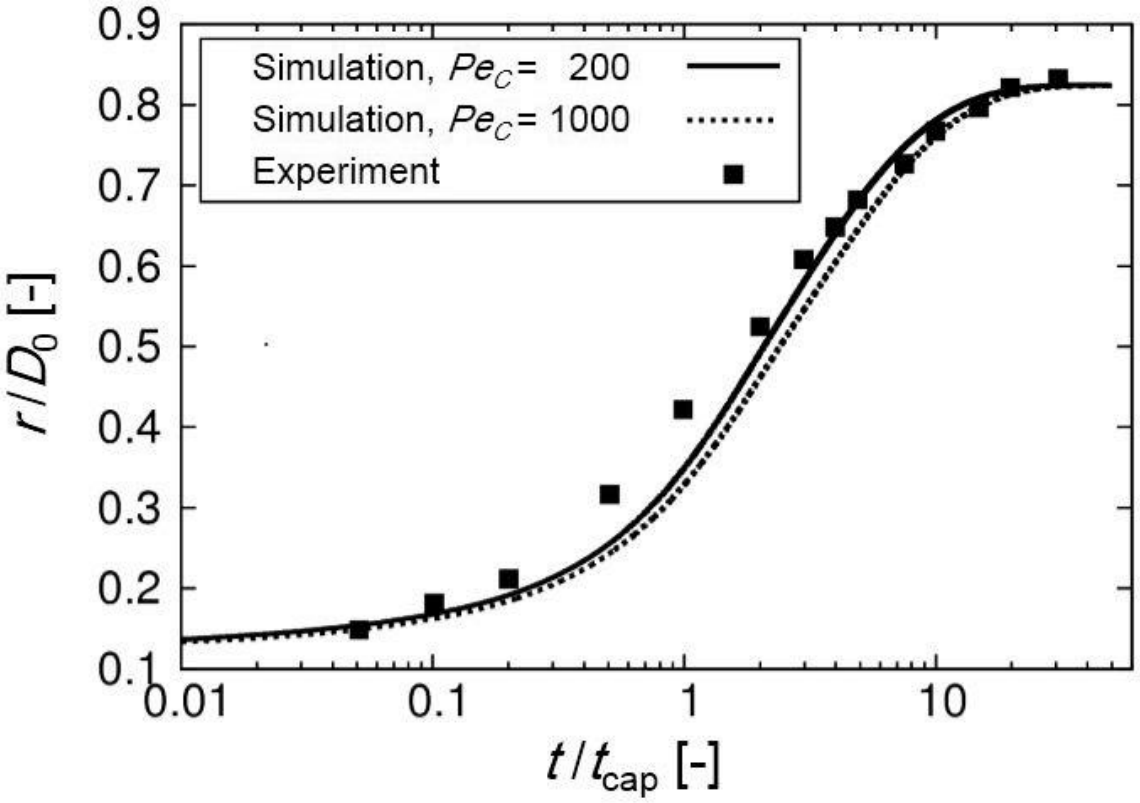

Fig. 4: Comparison of the temporal evolution of the computed droplet's base radius with experimental data [22] ($\theta_e = 58°$).

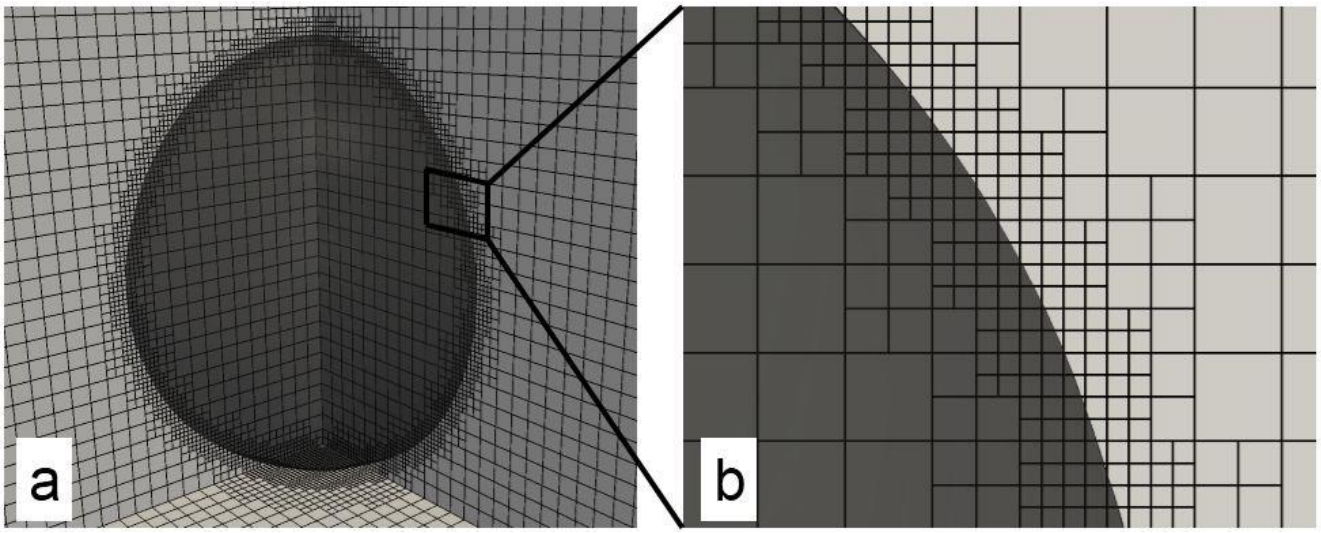

Fig. 5: (a) 3D AMR simulation of droplet spreading (one-quarter geometry, hexahedral mesh) on a flat substrate at the initial state. (b) Close-up view of the region with two-level AMR around the interface.

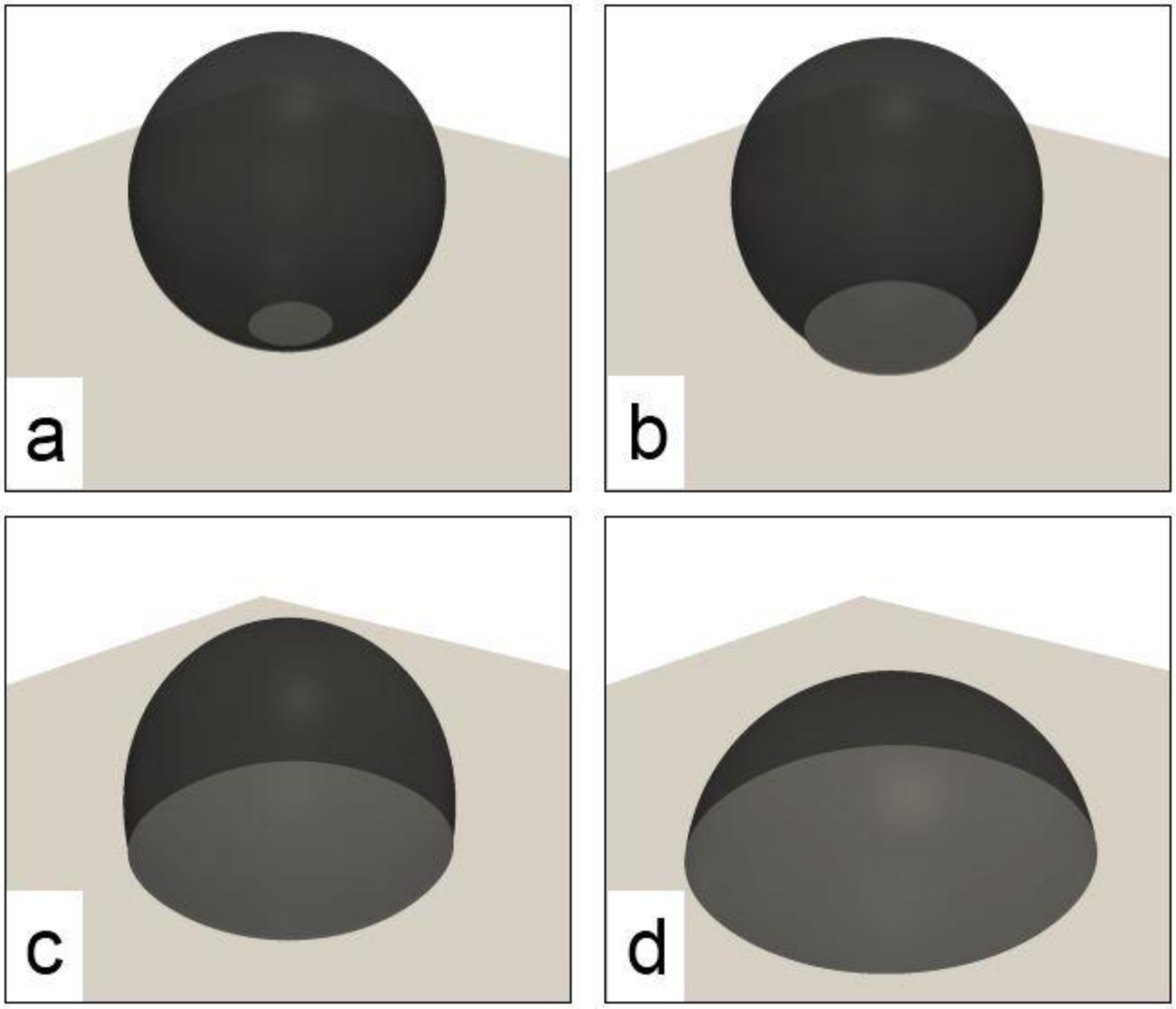

Fig. 6: 3D simulation of droplet spreading on a flat substrate ($\theta_e = 75°$) with AMR near the interface. Visualization of the droplet shape for different instants in time: (a) $t = 0$, $\theta_0 = 170°$ (initial state), (b) $t / t_{cap} = 2$, (c) $t / t_{cap} = 8$, (d) $t / t_{cap} = 30$ (equilibrium shape).

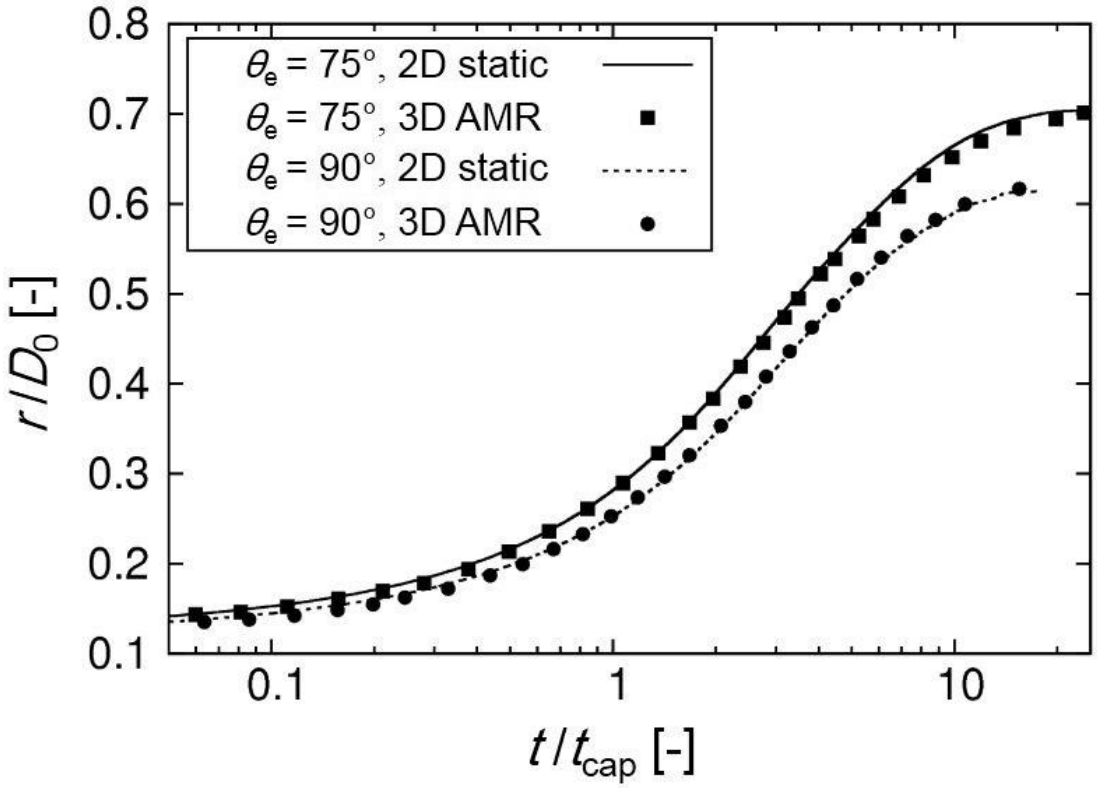

Fig. 7: Comparison of temporal evolution of droplet's base radius in 2D static mesh axisymmetric simulations and 3D AMR simulations.

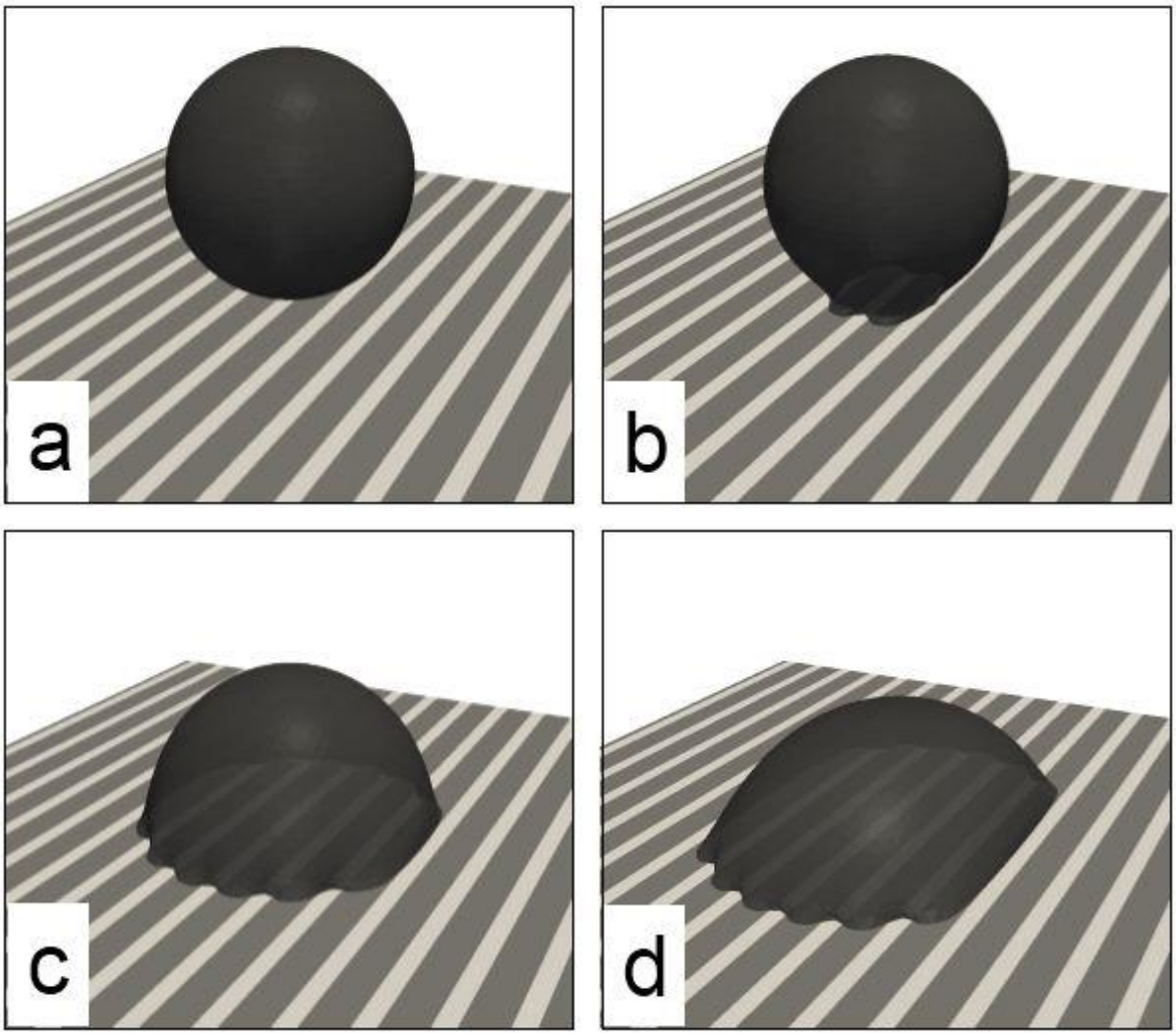

Fig. 8: Simulation of droplet spreading on a chemically patterned substrate (dark stripes: $\theta_e = 40°$, light stripes: $\theta_e = 110°$). The spreading process starts from initial state $t = 0$ (a), via $t / t_{cap} = 40$ (b) and $t / t_{cap} = 200$ (c), till $t / t_{cap} = 1000$ (d) where the droplet reaches the equilibrium state.

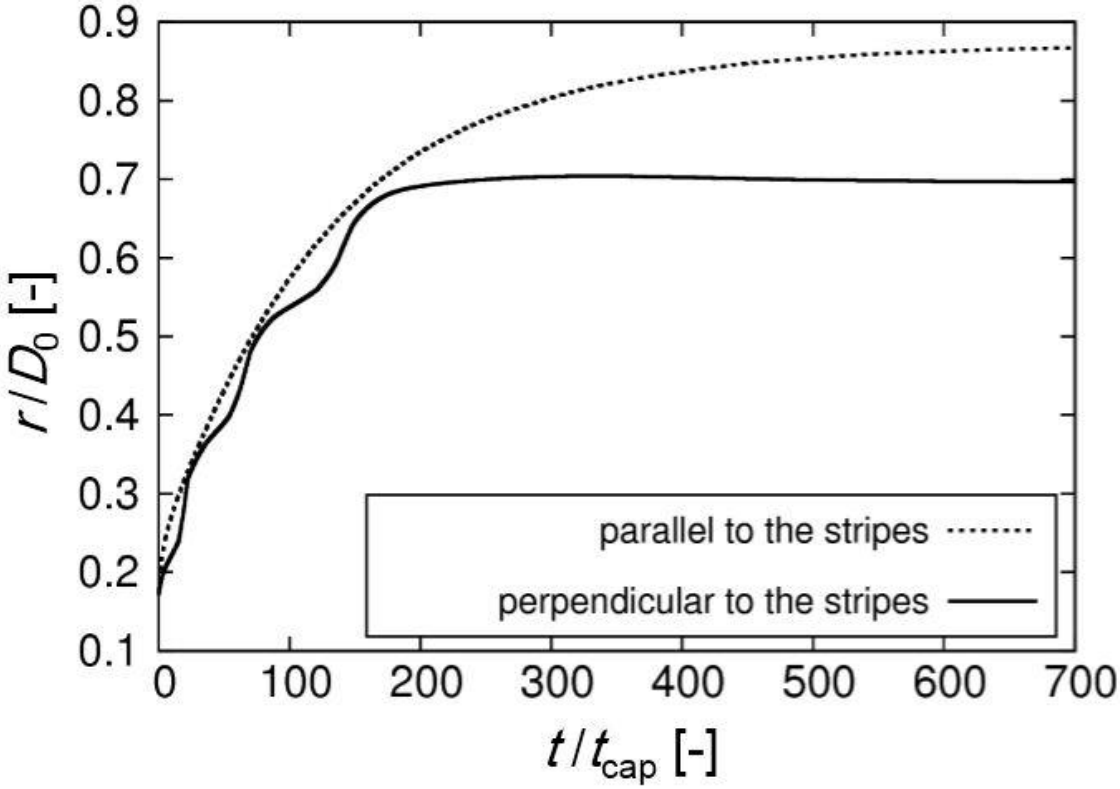

Fig. 9: Temporal evolution of the base radius of the droplet in direction parallel and perpendicular to the stripes.

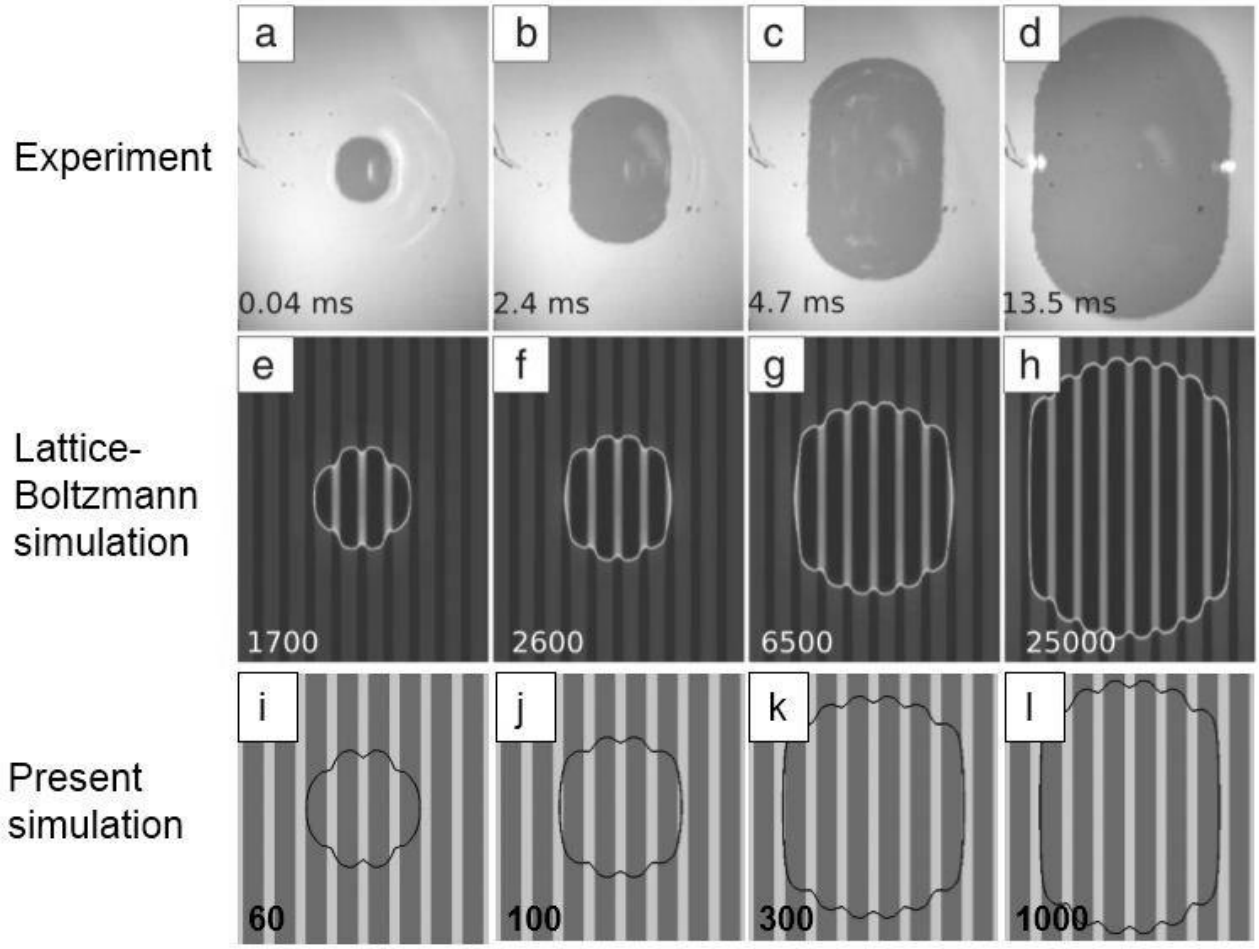

Fig. 10: Time evolution of the droplet shape from bottom-view. (a)-(h): Experiment and LB simulation. Reprinted figure with permission from H.P. Jensen et al., Phys Rev E 88, 013008 (2013) Copyright (2013) by the American Physical Society. (i)-(l): Present results. The numbers at the bottom left corner in subfigures (e)-(h) indicate the time step in the LB simulation while those in subfigures (i) – (l) denote t / t_{cap}.